Journal of Materials Chemistry A

ROYAL SOCIETY OF CHEMISTRY

PAPER

View Article Online
View Journal

Cite this: DOI: 10.1039/d3ta00942d

Activating the paddle-wheel effect towards lower temperature in a new sodium-ion solid electrolyte, $Na_{3.5}Si_{0.5}P_{0.5}Se_4$†

Yu Yang,[a] Zhenming Xu,[b] Chaohong Guan,[a] Runxin Ouyang,[a] Huirong Jing[a] and Hong Zhu *[a]

Received 16th February 2023
Accepted 29th March 2023

DOI: 10.1039/d3ta00942d

rsc.li/materials-a

Designing solid electrolytes with high room temperature (RT) conductivity is essential for the development of the next generation of solid-state batteries. Beyond the static structural framework, interaction between cation mobility and anion dynamics, *i.e.*, the paddle-wheel mechanism, may be the principle for enhanced cation mobility in solid electrolytes. Herein, we use first-principles calculations to study a promising polyanion-based solid electrolyte, Na_4SiSe_4, which meets the requirements of high ionic conductivity, and thermodynamic and dynamic stability simultaneously. *Ab initio* molecular dynamics reveal the fast Na diffusion dominated by the paddle-wheel mechanism, which is rationalized by the coupling of the translational motion of Na with the rotational motion of $SiSe_4$ in terms of time-space, vibrational properties, and energetics. Furthermore, by substituting Si with P, we theoretically predict $Na_{3.5}Si_{0.5}P_{0.5}Se_4$ with the paddle-wheel effect activated at 600 K, while Na_4SiSe_4 is activated at 1000 K. The calculated RT ionic conductivities of $Na_{3.5}Si_{0.5}P_{0.5}Se_4$ is up to 16.94 mS cm^{-1}. Our findings highlight that high cation mobility can be achieved by exploiting the anion rotation to invoke the paddle-wheel effect, especially in the low temperature range.

Introduction

Driven by the urgent need for the transition from fossil fuels to green energy, technological innovations in rechargeable batteries are eagerly sought.[1–3] By replacing flammable organic liquid electrolytes with solid electrolytes (SEs) and using a high-voltage cathode, solid-state batteries are expected to achieve greater safety and higher energy densities.[4] As an essential component of the solid-state battery, an ideal SE needs to have high ionic conductivity, low electronic conductivity, and electrochemical, chemical, and mechanical compatibility with the electrodes.[5] Many fundamental principles and design principles have been proposed for the development of SEs with high ionic conductivity ($\geq 10^{-3}$ S cm^{-1} at working temperatures), including crystal structure framework,[6–8] concerted migration,[9,10] lattice dynamics,[11–13] anion charge and volume,[14,15] and defect chemistry.[16–18] While previous understandings are mainly proposed from the perspective of static structural properties of the lattice, the anion dynamics (reorientation/rotation) that increase cation diffusivity are relatively less explored.[19]

It has been reported long ago that in some structures containing polyanions with covalent bonds such as sulfate (SO_4^{2-}), nitrate (NO_2^-), and phosphate (PO_4^{3-}), the cation conductivity can be increased by several orders of magnitude, which is ascribable to the activation of the reorientation/rotational motion of the polyanions during the order–disorder transformation into the superionic high-temperature (HT) phases.[20–22] The strong dynamic coupling between the reorientation/rotation of the polyanions and the cation translation was called the "paddle-wheel" mechanism.[20,23] Neutron diffraction, quasi-elastic neutron scattering (QENS), *ab initio* molecular dynamics simulations (AIMD), and other techniques have been applied to reveal the paddle-wheel effect.[24–27] More recently, the paddle-wheel effect in SEs has received growing attention. Zhang *et al.* proved that the rotational motion of PS_4^{3-}/PSe_4^{3-} polyanion couples to and facilitates the long-range cation mobility in $Na_{11}Sn_2PX_{12}$ (X = S, Se).[28] Subsequently, they found that the partial substitution of a "faster" polyanion (SiS_4^{4-}) for a "slower" one (PS_4^{3-}) is related to increased cation diffusivity in β-Li_3PS_4.[29] Wu *et al.* found that substituting Y^{3+} in Na_3YCl_6 with Zr^{4+} promotes polyanion rotation and increases Na^+ diffusivity.[5] Similarly, the cluster anion (*e.g.*, BH_4^- and OH^-) rotation facilitating the cation motion was observed in some other systems, such as argyrodite and antiperovskite.[30,31]

[a]University of Michigan–Shanghai Jiao Tong University Joint Institute, Shanghai Jiao Tong University, 800, Dongchuan Road, Shanghai 200240, China. E-mail: hong.zhu@sjtu.edu.cn

[b]College of Materials Science and Technology, Nanjing University of Aeronautics and Astronautics, Nanjing 210016, China

† Electronic supplementary information (ESI) available: The species projected MSD; radial distribution function; van Hove correlation function; displacement plots; vibrational modes; phonon dispersions; density of states; structural information; power spectrum; Bader charge. See DOI: https://doi.org/10.1039/d3ta00942d

Table 1 Some reported superionic conductors with anion rotation[a]

System	AIMD temperature (K) with anion rotation	Paddle-wheel effect	Ref.
$Na_{11}Sn_2PX_{12}$ (X = S, Se)	>600	Yes	28
β-Li_3PS_4; $Li_{3.25}Si_{0.25}P_{0.75}S_4$	>900	Yes	29
$Na_{2.25}Y_{0.25}Z_{0.75}Cl_6$	>600	—	5
$Li_2(OH)_{0.9}F_{0.1}Cl$	1100	—	31
$Li_6PS_5BH_4$	600	No	32

[a] Note: denotes whether paddle-wheel effects exist or not is not confirmed in the reference.

As an exception, Sun *et al.* demonstrated that the enhanced conductivity in BH_4^- substituted Li argyrodite mainly derives from the weak interaction between Li and BH_4^- polyanions instead of the usually expected paddle-wheel effect rising from cluster-ion rotation.[32] Therefore, the presence of polyanions or cluster ions in SE is a prerequisite for anion rotation, but whether anion rotation accelerates cation translation motion and displays paddle-wheel effects needs to be discussed in depth. It is worth noting that the paddle-wheel phenomenon was only reported for AIMD simulations above 600 K (Table 1). It makes more sense to introduce the paddle-wheel effect into the low temperature range that is more relevant to solid-state battery applications. Of course, due to the short times of AIMD simulations, accurate determination of the onset temperature of anion reorientation/rotation should rely on experimental techniques.

In this work, we investigated a potential solid electrolyte, Na_4SiSe_4, which was found to have good thermodynamic and dynamic stability by density functional theory calculations. More importantly, *ab initio* molecular dynamics (AIMD) simulations provide a comprehensive insight into the coupling between the translational motion of cations and the rotational motion of anions. The Na translation and $SiSe_4$ rotation are proved to be correlated in time-space, vibrational properties, and energetics. In addition, we generated P-substituted $Na_{3.5}Si_{0.5}P_{0.5}Se_4$, whose paddle-wheel effect is activated at 600 K, whereas Na_4SiSe_4 is activated at 1000 K. The calculated room temperature ionic conductivities of Na_4SiSe_4 and $Na_{3.5}Si_{0.5}P_{0.5}Se_4$ are 1.42 and 16.94 mS cm^{-1}, respectively, implying that they are promising superionic conductors. Our findings elucidate that high cation mobility can be achieved by exploiting anion rotation to invoke the paddle-wheel mechanism, especially in the low temperature range.

Results and discussion

Structure and stability

As we mentioned in the Introduction section of the paper, the solid electrolytes $Na_{11}Sn_2PX_{12}$ (X = S, Se), β-Li_3PS_4 and Na_3YCl_6 all satisfy the condition of isolated polyanions, *i.e.*, there are no common vertices between non-lithium cation polyhedra, and this isolated arrangement provides degrees of freedom for the rotation of the polyanion. By screening the Materials Project (MP) database[33,34] for structures with isolated polyanions which can potentially rotate easily (small electronegativity difference between the vertex and center atom of the polyanion), we found the orthorhombic Na_4SiSe_4 (mp-30931, ICSD[35] ID: 409726). Na_4SiSe_4 (Fig. 1) has three inequivalent Na^{1+} sites in the unit cell, which form square plane (Na^{I}), square pyramidal (Na^{II}), and trigonal bipyramid (Na^{III}) with Se^{2-}, respectively. The flexible Na^{1+} coordination environment may promote the disordered sublattice as well as the Na vacancy/interstitial formation.[36] Si^{4+} is bonded in a tetrahedral geometry to four Se^{2-} atoms. DFT-optimized lattice parameters of Na_4SiSe_4 are listed in Tables S1 in the ESI.†

A promising SE must meet a set of stringent requirements. First, the thermodynamic stability was evaluated by comparing the energy of Na_4SiSe_4 with that of all the available combinations of competing phases (the convex hull construction).[37] Fig. 2a shows that the E_{hull} value of Na_4SiSe_4 is 0.74 meV per atom, and such a low E_{hull} value implies that Na_4SiSe_4 is thermodynamically stable at 0 K. In addition, there are no imaginary frequencies in phonon dispersions (Fig. 2b), indicating that Na_4SiSe_4 is dynamically stable at 0 K in the harmonic approximation. Importantly, the orthorhombic Na_4SiSe_4 phase has been synthesized experimentally,[38] which is consistent with the results of our calculations.

The electronic density of states of Na_4SiSe_4 is shown in Fig. 2c. The valence band maximum is dominated by Se^{2-}, which is the first element to be oxidized at high voltages. The calculated band gap of Na_4SiSe_4 is 3.09 eV, which can

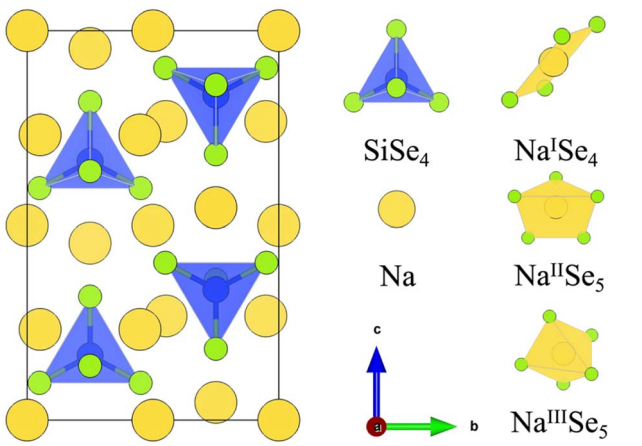

Fig. 1 Unit cell of orthorhombic Na_4SiSe_4. Na atoms are depicted as yellow spheres, Se as green spheres, and $SiSe_4$ as bule tetrahedra.

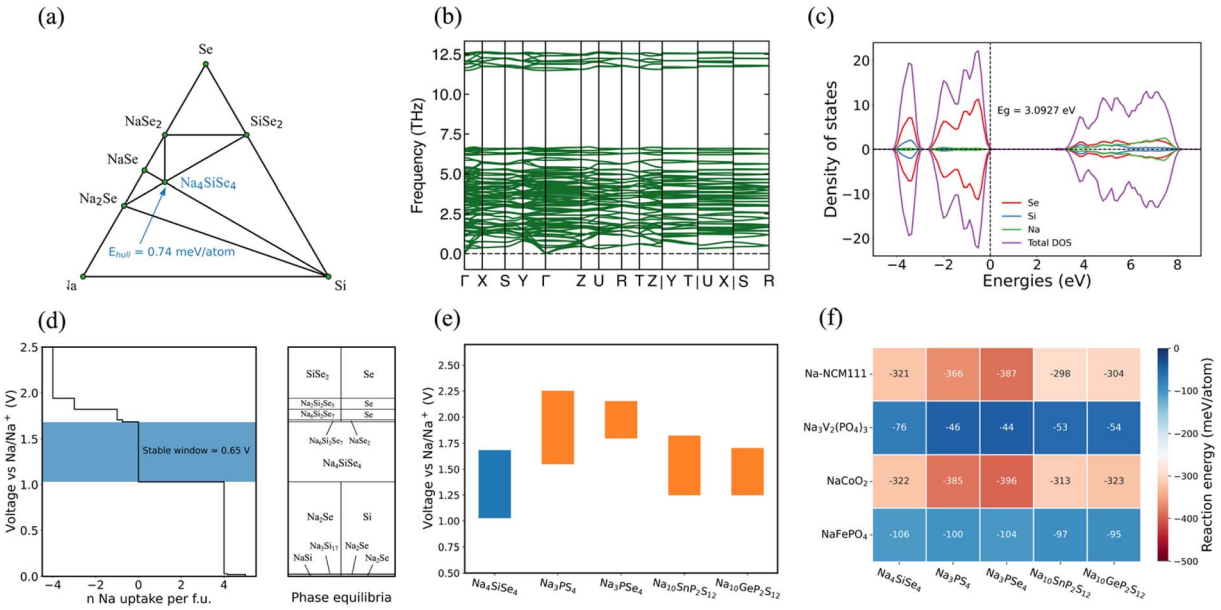

Fig. 2 Thermodynamic, dynamic, electrochemical, and chemical stabilities of Na_4SiSe_4. (a) Na–Si–Se phase diagram; the green dots represent the stable compounds. (b) Phonon dispersions of Na_4SiSe_4. (c) Density of states and band gap (E_g) of Na_4SiSe_4. (d) Voltage profile (with respect to the chemical potential of Na metal) and phase equilibria of Na_4SiSe_4 upon Na insertion ($n > 0$) and Na extraction ($n < 0$). (e) Electrochemical windows of Na_4SiSe_4 and other sodium superionic conductors. (f) Reaction energies ΔE_D (interface) between Na_4SiSe_4 and four typical cathodes ($NaNi_{1/3}Co_{1/3}Mn_{1/3}O_2$, $Na_3V_2(PO_4)_3$, $NaCoO_2$, and $NaFePO_4$), compared with four other typical sodium superionic conductors.

effectively insulate electron transport. It is important to note that the value of the band gap only represents the upper limit of electrochemical stability; a wide band gap does not always lead to a wide electrochemical window.[39] The electrochemical stability window was calculated based on the grand potential phase diagram as a function of Na chemical potential,[40] as shown in Fig. 2d. The stable electrochemical window of Na_4SiSe_4 is 0.65 V, ranging from 1.03 to 1.68 V. The window size is comparable to that of $Na_{10}Sn_2PS_{12}$ and $Na_{10}GeP_2S_{12}$, but the oxidation and reduction potentials are slightly lower, as shown in Fig. 2e. The chemical stability of Na_4SiSe_4 was assessed by calculating its reaction energy with the cathode materials, as shown in Fig. 2f. Na_4SiSe_4 exhibits relatively low reaction energies (−76 meV per atom) against $Na_3V_2(PO_4)_3$, indicating that $Na_3V_2(PO_4)_3$ is the most suitable cathode for the system we studied. The reaction energy between the Na_4SiSe_4 and $NaNi_{1/3}Co_{1/3}Mn_{1/3}O_2$ and $NaCoO_2$ cathode materials are −321 and −322 meV per atom, respectively, which may lead to chemical decomposition at the interface.[41] In summary, Na_4SiSe_4 has good thermodynamic and dynamic stability and its electrochemical and chemical stability is comparable to that of common sulfide electrolytes.

Origin of fast Na ion diffusion in Na_4SiSe_4

To study the diffusion mechanism of Na in Na_4SiSe_4, AIMD simulations were performed at elevated temperatures ranging from 900 K to 1500 K at 100 K intervals. The species projected mean-square displacement (MSD) plots in Fig. S1 in the ESI† shows that the framework does not melt during the simulations. The Na MSD plot in Fig. 3a shows that the diffusivity of Na increases with increasing temperature and undergoes a significant change (4.73×10^{-6} to 2.41×10^{-5} $cm^2\ s^{-1}$) from 900 K to 1000 K. To characterize the $SiSe_4$ polyanion dynamics, we calculated the reorientation autocorrelation function $C(t)$ (see Methods for details) of $SiSe_4$, as shown in Fig. 3b. The $SiSe_4$ $C(t)$ is approximately equal to 1 at 900 K, indicating that the orientations of $SiSe_4$ remain "fixed" near their initial orientations.[42] However, the $SiSe_4$ $C(t)$ experiences a pronounced decay at temperatures above 1000 K, implying that the rotational motion of $SiSe_4$ is activated at 1000 K. This trend is verified by the probability density analysis.[43] At 900 K, the Na trajectories (left panel in Fig. 3c) indicate mostly local Na vibration with almost no long-range transport, consistent with the observed low Na diffusivity; meanwhile, the Se atom (right panel in Fig. 3c) vibrates near their initial position, in agreement with $C(t)$ analysis. In contrast, macroscopic three-dimensional Na diffusion (left panel in Fig. 3d) is observed at 1000 K, accompanied by rotational motion of $SiSe_4$ (the Se trajectories resembling a cage surrounding the Si, right panel in Fig. 3d). From the above analysis, we found that the fast Na ion conduction and the rotational motion of $SiSe_4$ are activated simultaneously at 1000 K. The rotational motion of $SiSe_4$ may facilitate the translational motion of Na.

Time-space coupling of Na translation and $SiSe_4$ rotation

To thoroughly elucidate the correlation between the rotational motion of $SiSe_4$ and the translational motion of Na, we calculated the functional $h_i(t, a, \Delta t, t_a)$,[44–46] which identifies long-lived Na displacements of at least a distance a occurring at time t:w

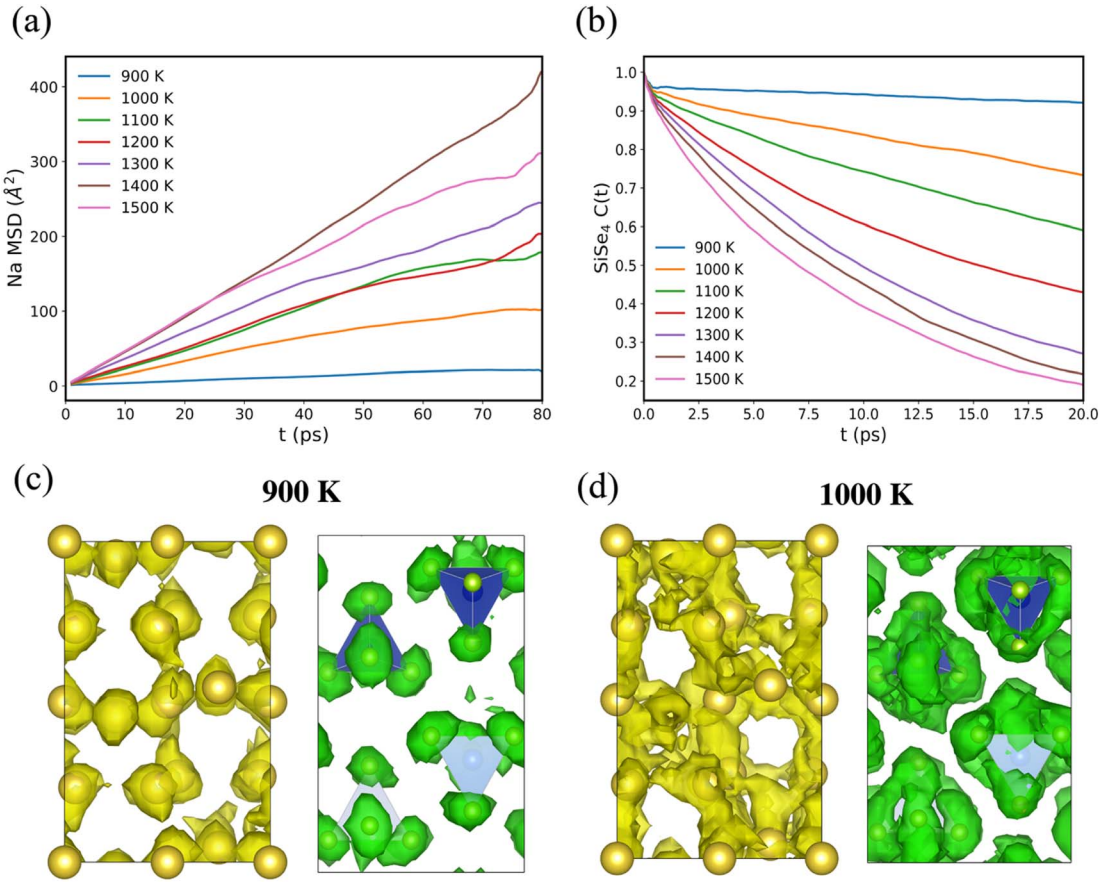

Fig. 3 Effect of temperature on Na diffusion and $SiSe_4$ reorientation/rotation in Na_4SiSe_4. (a) Na MSD and (b) $SiSe_4$ reorientation autocorrelation function $C(t)$ as a function of temperature. The probability density of Na (yellow iso-surface) and Se (green iso-surface) (c) at 900 K, and (d) at 1000 K, and the iso-surface value is set to $2P_0$ where P_0 is defined as the mean value of the density.

$$h_i(t;\ a,\ \Delta t,\ t_a) = \prod_{t'=\frac{t_a}{2}-\Delta t}^{\frac{t_a}{2}} \theta\left(\left|r_i(t+t') - r_i(t-t')\right| - a\right) \quad (1)$$

here $\theta(x)$ is the Heaviside step function, and $\theta(x) = 1$ or 0 for $x \geq 0$ or <0, respectively. $r_i(t)$ represents the displacement of atom i at time t. a is a displacement cutoff. $\Delta t = 3$ ps, is the residence time before and after the displacement event and ensures that these displacements are long lived. $t_a = 9$ ps, is a longer time window, including the residence and transition times. When $h_i = 1$ it represents that the atom i undergoes such a displacement; otherwise, $h_i = 0$. For our analysis, $a = 3.8$ Å, which is the approximate Na–Na average distance (see radial distribution function in Fig. S2†).

Each rectangle in Fig. 4a individually plots h_i (eqn (1)) *vs.* simulation time for the 48 Na ions contained in the simulation cell during the second 20 ps trajectory at 1000 K (the data for the other simulation time periods are described below). We identified that a total of 12 Na ions underwent long-lived migration events. Summing the h_i for all Na ions at each time t enables the identification of ions whose migration events occur simultaneously (or near simultaneously), as shown in Fig. 4b. A minimum of two and a maximum of six Na migration events are correlated in time. However, are these events also correlated in space? We calculated and plotted the distinct-part of the van Hove correlation function[43] (G_d) for the Na–Na pair at 1000 K, as shown in Fig. S3.† G_d only exhibits a few sparse peaks at the proximity of $r = 0$, implying that the Na ion motions are uncorrelated in space. The Na ion migration mechanism of Na_4SiSe_4 differs from that of typical fast ion conductors, such as cubic-phase $Li_7La_3Zr_2O_{12}$ (LLZO) and $Li_{10}GeP_2S_{12}$ (LGPS), where the concerted migration mechanism[9] of cation is observed.

A cooperative migration event involving three Na ions (identified with blue shading in Fig. 4a, Na IDs are 17, 18 and 19) is used to visualize the motion of the cation and anion. Fig. 4c shows the position of the three Na ions and their two nearest-neighbor $SiSe_4$ polyanions, a total of 9 ps trajectory before and after the cooperative migration event occurs. It can be seen that in addition to the translational motion of Na, its surrounding $SiSe_4$ also underwent a degree of rotational motion. Fig. 4d illustrates the translational displacement (unit in Å) of the three Na ions and the rotational displacement (unit in °) of their two nearest-neighbor $SiSe_4$ polyanions in the cooperative migration event depicted in Fig. 4c. The translational displacement of the Na is displayed as black lines on

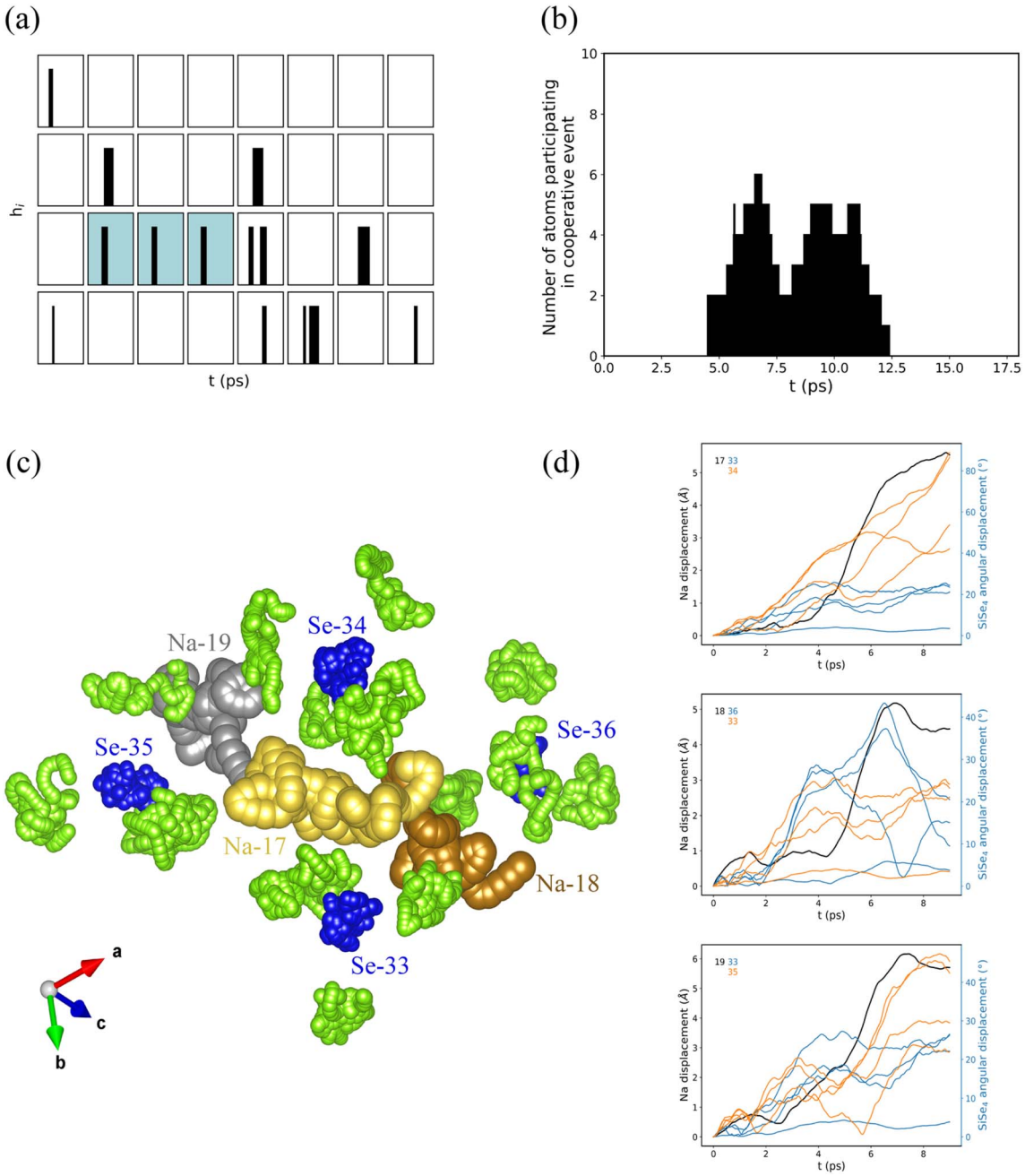

Fig. 4 Characterization of Na migration events, and their correlation with rotational displacements of a $SiSe_4$ polyanion, in Na_4SiSe_4 during the second 20 ps trajectory at 1000 K. (a) Identification of individual Na-ion migration events. Each rectangle individually plots h_i (eqn (1)) *vs.* simulation time for the 48 Na ions in the simulation cell. (b) Number of Na atoms participating in the cooperative migration event as a function of the time at which those events were observed. (c) Illustration of the cooperative Na migration event (identified with blue shading in (a)), and the trajectory of its surrounding $SiSe_4$ polyanion. The silver, yellow and brown spheres represent the positions of the three different Na in the 9 ps trajectory. Si and Se are labelled as blue and green spheres, respectively. Colored numeric labels identify the ID of atoms. (d) Displacements of Na-ions (black line, left axis) that are involved in the cooperative migration event (identified with blue shading in (a) and illustrated in (c)) and the angular displacements of the two nearest-neighbor $SiSe_4$ polyanions (blue and orange line, right axis). The ID for each Na and $SiSe_4$ polyanion is marked in the top left corner of each plot. Four rotational displacements are plotted for each $SiSe_4$ polyanion using the same color, corresponding to the rotation of the four Se atoms around the center of mass of the $SiSe_4$ polyanion. To identify long-lived Na displacements more clearly (to differentiate them from local vibrations), the atom positions in (d) are averaged over a moving time window of width equal to 2 ps.

the left axis, while the rotational displacements of the two nearest-neighbor $SiSe_4$ are displayed as blue and orange lines on the right axis. Four rotational displacements are shown for each $SiSe_4$ polyanion using the same color, corresponding to the rotation of the four Se atoms around the center of mass of the $SiSe_4$ polyanion. There is a strong correlation between the

displacement of Na and the rotational displacement of $SiSe_4$, and this is demonstrated by the fact that the displacements of Na and $SiSe_4$ occur at similar times and have a common shape in the displacement plots. Displacement plots for all migration events in Fig. 4a and from the other simulation time periods at 1000 K are shown in Fig. S4–S6.† These data (a total of 60 ps of simulation time) show that in approximately 30% (13 out of 41 events) of the events, the $SiSe_4$ rotational displacement precedes the Na displacement. With three exceptions (Na displacement precedes $SiSe_4$ rotational displacement), the remaining events show that Na displacement and $SiSe_4$ rotational displacement occurred simultaneously. The displacement curves of Na and $SiSe_4$ exhibit a similar trend. In addition, large and sustained rotational displacements (35–100°) of $SiSe_4$ were observed. Similar behavior is seen in the prototype glass ($75Li_2S$–$25P_2S_5$) with the paddle-wheel effect.[46] The above shows that Na translation and $SiSe_4$ rotation are coupled in time and space.

Vibrational properties and energetics coupling of Na translation and $SiSe_4$ rotation

To gain a more generic understanding on the correlation between the rotational motion of $SiSe_4$ and the translational motion of Na, the power spectrum (see Methods for details) was calculated to characterize the vibrational properties. Fig. 5a shows the power spectrum of Na vibration and $SiSe_4$ libration at 300 K in Na_4SiSe_4. The vibration spectrum of Na shows a peak near 3–4 THz, corresponding to the Na translational modes (see typical vibrational modes in Fig. S7†), while the libration spectrum of $SiSe_4$ has a peak near 1–2 THz, corresponding to the $SiSe_4$ rotational modes (Fig. S7†). The spectrum of Na and $SiSe_4$ have a large overlap (grey shades) in the low frequency region (1–5 THz), indicating that the rotational motion of $SiSe_4$ is coupled to the translational motion of Na and that the anharmonic thermal libration of the $SiSe_4$ may transfer momentum to the Na prior to migration events.

From an energetic perspective, we plotted the Arrhenius plots of the translational diffusivity of Na and the rotational diffusivity of $SiSe_4$, as shown in Fig. 5b. It is important to note that the Na diffusion coefficient and the $SiSe_4$ rotational diffusion coefficient were calculated using the Green–Kubo formula (see Methods for details).[58] The calculated activation energy for $SiSe_4$ rotation is 0.37 eV, which is slightly greater than the translation activation energy of Na, 0.29 eV. A similar pattern has been shown in some of the materials with paddle-wheel effects. For instance, in the prototype glass ($75Li_2S$–$25P_2S_5$), PS_4 exhibits a rotational activation energy of 0.27 eV, which is comparable to, but slightly larger than that for Li translation, 0.22 eV.[46] In addition, in sulfates (Li_2SO_4), the rotational activation energy for SO_4 is 0.40 eV, which is similar to, but slightly larger than that for Li diffusion, 0.34 eV.[47] Therefore, we infer that in Na_4SiSe_4, the rotation motion of $SiSe_4$ and the translational motion of Na are energetically coupled.

Based on the above discussion, we demonstrate that in Na_4SiSe_4, the rotational motion of $SiSe_4$ and the translational motion of Na are strongly correlated in time-space, vibrational properties, and energetics, which is consistent with the paddle-wheel mechanism. Furthermore, Na diffusion and $SiSe_4$ rotation are activated simultaneously at 1000 K, implying that the motion of Na ions is strongly dependent on the rotation of $SiSe_4$. There is almost no Na vacancy/interstitial diffusion at temperatures below 1000 K, and no concerted migration mechanism[9] of Na is observed at high temperatures, suggesting that the diffusion of Na in Na_4SiSe_4 is dominated by the paddle-wheel mechanism.

Regulating the paddle-wheel effect to a lower temperature

Although we discovered fast Na ion conduction with low energy barriers (0.29 eV, Fig. 5b) dominated by the paddle-wheel mechanism in Na_4SiSe_4, this effect is only triggered at temperatures above 1000 K. In contrast, anion rotation in some reported SEs is activated only at 600 K. It is necessary to regulate the paddle-wheel effect in Na_4SiSe_4 to a lower temperature range. In general, the large free volume in lattice and highly covalent bonds in polyanions are conducive to the rotation of

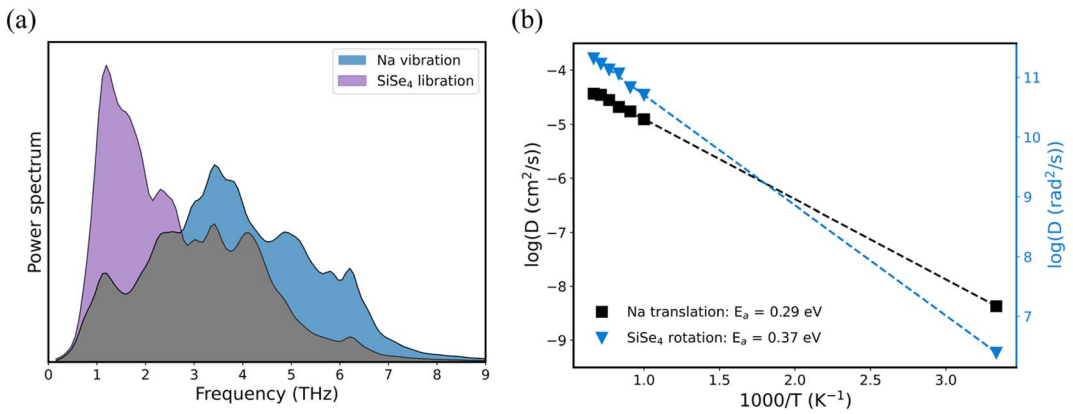

Fig. 5 (a) Power spectrum calculated *via* the Fourier transform of linear velocity autocorrelation for Na (bule) and angular velocity autocorrelation for $SiSe_4$ (purple) at 300 K in Na_4SiSe_4. (b) Calculated Arrhenius plots and activation energies using the Green–Kubo formula for $SiSe_4$ rotational diffusion (blue triangles, right axis) and Na translational diffusion (black squares, left axis) in Na_4SiSe_4. The dashed lines are a linear fit to the data at 1000 to 1500 K. Values at 300 K are extrapolated from the high temperature data.

the anion.[19] Here, we generated a P-substituted $Na_{3.5}Si_{0.5}P_{0.5}Se_4$ structure because the electronegativity difference between P and Se is smaller than that of Si and Se. Pymatgen code[48] was used to enumerate possible arrangements based on the electrostatic energy criteria;[49] then 20 structures with the lowest electrostatic energy were selected and relaxed, and the one with the lowest DFT energy was selected as the representative ground-state structure for $Na_{3.5}Si_{0.5}P_{0.5}Se_4$. DFT-optimized lattice parameters of $Na_{3.5}Si_{0.5}P_{0.5}Se_4$ are listed in Table S2.† The E_{hull} value of $Na_{3.5}Si_{0.5}P_{0.5}Se_4$ is calculated to be 16 meV per atom, which is sufficiently small (below 25 meV per atom) that $Na_{3.5}Si_{0.5}P_{0.5}Se_4$ can be easily stabilized by entropic effects at elevated temperatures or created as metastable phases. No imaginary vibrational mode is observed from the phonon dispersions (Fig. S8†), which means that $Na_{3.5}Si_{0.5}P_{0.5}Se_4$ is dynamically stable. In addition, the calculated band gap of $Na_{3.5}Si_{0.5}P_{0.5}Se_4$ is 2.87 eV (Fig. S9†), which is comparable to, but slightly less than that of Na_4SiSe_4.

Likewise, the $C(t)$ was calculated from AIMD simulations to study anion dynamics in $Na_{3.5}Si_{0.5}P_{0.5}Se_4$, as shown in Fig. 6a. At 500 K, $SiSe_4$ hardly undergoes rotation/reorientation and PSe_4 has a very slight rotation, while the $C(t)$ of both $SiSe_4$ and PSe_4 undergo a significant decay from 600 K to 900 K; meanwhile, Na also undergoes significant diffusion (see MSD plots in Fig. S10†), implying that the paddle-wheel effect is activated at 600 K for $Na_{3.5}Si_{0.5}P_{0.5}Se_4$. Interestingly, PSe_4 (dashed lines) shows a faster rotation than $SiSe_4$ (solid lines) at all temperatures. This is because PSe_4 has a smaller partial charge difference between the anion and the central atoms than that of $SiSe_4$ (Bader analysis in Table S3†), which is consistent with the qualitative Pauling electronegativity scale. The more covalent nature of the P–Se bond contributes to the easier and faster rotation of PSe_4. Compared to Na_4SiSe_4 (>1000 K), $Na_{3.5}Si_{0.5}P_{0.5}Se_4$ enables the paddle-wheel effect in a lower temperature range (>600 K). Fig. 6b and Table S4† show that the calculated RT ionic conductivities of Na_4SiSe_4 and $Na_{3.5}Si_{0.5}P_{0.5}Se_4$ are 1.42 and 16.94 mS cm^{-1} with activation energies of 0.279 and 0.195 eV, respectively. The coefficient D was calculated using the Einstein formula (see Methods for details) as in previous studies.[50] As expected, the Na diffusion activation energy of Na_4SiSe_4 calculated by using the Einstein formula (0.279 eV) and Green–Kubo formula (0.29 eV, Fig. 5b) is comparable. Compared with the previously calculated sodium-ion solid electrolytes $Na_{11}Sn_2PS_{12}$ (ref. 51), $Na_7P_3S_{11}$ (ref. 52) and $Na_{2.875}PS_{3.875}Cl_{0.125}$ (ref. 53), $Na_{3.5}Si_{0.5}P_{0.5}Se_4$ shows the highest RT ionic conductivity and the lowest activation

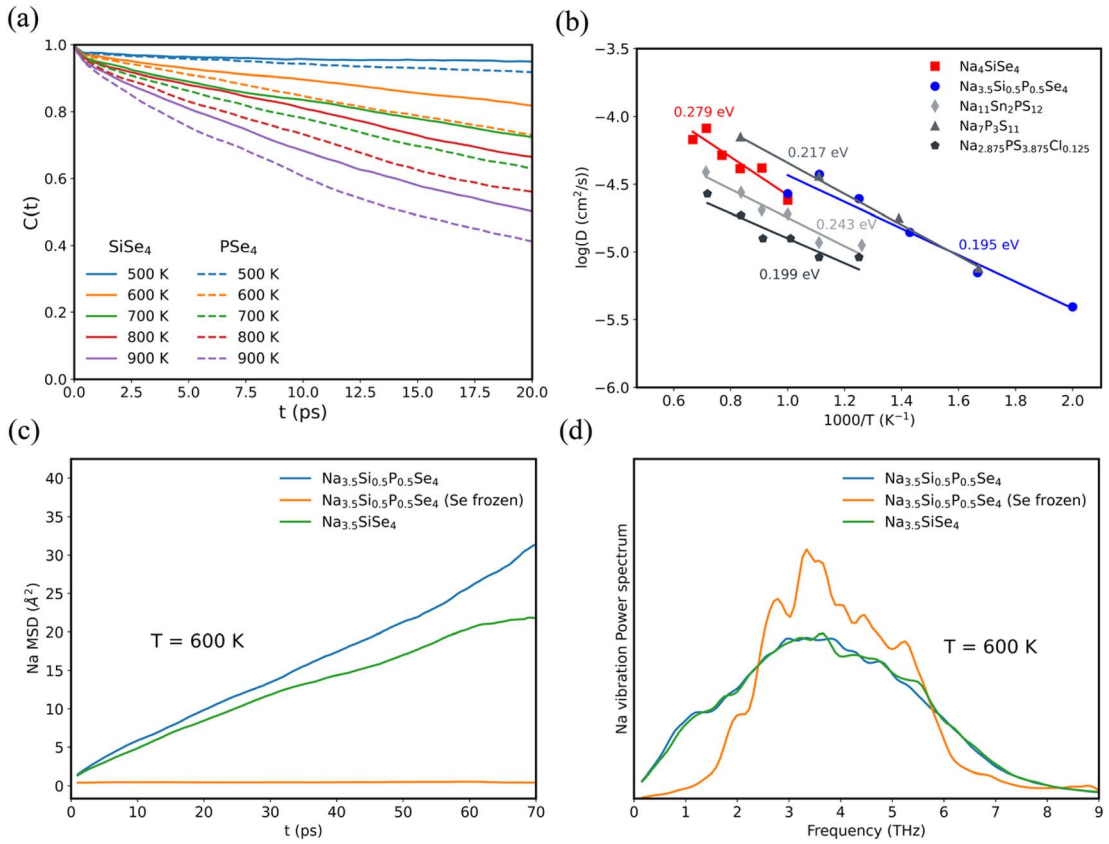

Fig. 6 (a) Reorientation autocorrelation function $C(t)$ for $SiSe_4$ (solid lines) and PSe_4 (dashed lines) as a function of temperature in $Na_{3.5}Si_{0.5}P_{0.5}Se_4$. (b) Arrhenius plot of the calculated diffusivities using the Einstein formula for Na_4SiSe_4 (red squares) and $Na_{3.5}Si_{0.5}P_{0.5}Se_4$ (blue circles). The calculated data of $Na_{11}Sn_2PS_{12}$ (ref. 51), $Na_7P_3S_{11}$ (ref. 52) and $Na_{2.875}PS_{3.875}Cl_{0.125}$ (ref. 53) were also plotted for comparison. (c) Na MSD at 600 K for $Na_{3.5}Si_{0.5}P_{0.5}Se_4$, $Na_{3.5}Si_{0.5}P_{0.5}Se_4$ (with the Se atom frozen) and $Na_{3.5}SiSe_4$. (d) Na vibration power spectrum at 600 K for $Na_{3.5}Si_{0.5}P_{0.5}Se_4$, $Na_{3.5}Si_{0.5}P_{0.5}Se_4$ (with the Se atom frozen) and $Na_{3.5}SiSe_4$.

energy, meaning that $Na_{3.5}Si_{0.5}P_{0.5}Se_4$ is a promising superionic conductor. We also examined the power spectrum in $Na_{3.5}Si_{0.5}P_{0.5}Se_4$ where a strong overlap between the Na translational modes and $PSe_4/SiSe_4$ rotational modes was also observed (Fig. S11†), indicating the coupling motion between cation diffusion and anion rotation.

Are the lower paddle-wheel activation temperature and enhanced conductivity of $Na_{3.5}Si_{0.5}P_{0.5}Se_4$ due to the newly introduced PS_4, or due to the effect of Na vacancies generated *via* charge compensation? We generated $Na_{3.5}SiSe_4$ with the same lattice parameters as the original structure of Na_4SiSe_4 based on the electrostatic energy criteria. AIMD simulations were then performed, with defect charges compensated by a uniform background charge. The $C(t)$ and Arrhenius plot of $Na_{3.5}SiSe_4$ are shown in Fig. S12.† $Na_{3.5}SiSe_4$ exhibits a similar behavior to that of $Na_{3.5}Si_{0.5}P_{0.5}Se_4$, with $SiSe_4$ undergoing a significant rotation from 600 K, with a low activation energy of 0.236 eV, implying that Na vacancies are critical for enabling the rotation of the polyanion. The volume per atom of $Na_{3.5}Si_{0.5}P_{0.5}Se_4$ (28.08 Å^3) is larger than that of Na_4SiSe_4 (27.06 Å^3) due to the presence of Na vacancies, providing more free volume for anion rotation. Furthermore, if we froze the Se atom in $Na_{3.5}Si_{0.5}P_{0.5}Se_4$ at 600 K, the Na MSD is almost 0 (Fig. 6c); meanwhile, the low frequency (0–2.5 THz) vibrational mode of Na also disappears (Fig. 6d), suggesting the decoupling of anion–cation dynamics. This demonstrates that the prerequisite for Na diffusion is the reorientation/rotation of Se rather than the presence of Na vacancies. Therefore, we have shown that the larger free volume generated by Na vacancies enables the rotation of the polyanion at lower temperatures and that the newly introduced PS_4 rotates faster than $SiSe_4$, both of which together contribute to the enhanced conductivity of $Na_{3.5}Si_{0.5}P_{0.5}Se_4$.

Conclusions

We investigated a potential solid electrolyte material, Na_4SiSe_4, which we have confirmed to have good thermodynamic and dynamic stability by DFT calculations. AIMD simulations were performed to gain insight into the diffusion mechanism of Na_4SiSe_4. We found that the diffusion of Na and the rotation of $SiSe_4$ were activated simultaneously at 1000 K. By identifying all Na migration events, we found that Na translational motion and $SiSe_4$ rotational motion are coupled in time and in space. Furthermore, we found that the power spectrum of Na vibration and $SiSe_4$ libration have a strong overlap in the low frequency region. Na translation and $SiSe_4$ rotation have a comparable activation energy. The paddle-wheel mechanism dominates the fast Na ion conduction in Na_4SiSe_4 with a RT ionic conductivity of 1.42 mS cm^{-1} and an activation energy of 0.279 eV. In addition, we calculated the P-substituted $Na_{3.5}Si_{0.5}P_{0.5}Se_4$ with a RT ionic conductivity of 16.94 mS cm^{-1} and an activation energy of 0.195 eV. Compared to Na_4SiSe_4 (>1000 K), $Na_{3.5}Si_{0.5}P_{0.5}Se_4$ enables the paddle-wheel effect in a lower temperature range (>600 K), which can be attributed to the larger free volume generated by Na vacancies. Our findings highlight that fast ion conduction can be achieved by exploiting the anion rotation to invoke the paddle-wheel mechanism, especially in the low temperature range.

Methods

All calculations were carried out in the framework of density functional theory (DFT)[54] using the projector augmented wave method,[55] as implemented in the Vienna *ab initio* Simulation Package (VASP). The generalized gradient approximation (GGA)[56] and Perdew–Burke–Ernzerhof (PBE) exchange functional were employed.[54] For structural optimization calculations, a plane-wave energy cutoff of 520 eV was used and the Brillouin zone was sampled by using a 4 × 3 × 2 Gamma-centered k-point grid. The convergence criteria of the energy and force are 1×10^{-5} eV and 0.01 eV Å^{-1}, respectively. Electronic structures are calculated using the HSE06 functional,[57] which is known to yield reliable band gap values. Phonon dispersions are calculated using the density functional perturbation theory (DFPT),[57] as implemented in the PHONOPY code.[59]

AIMD calculations were performed without spin-polarization in an NVT canonical ensemble at elevated temperatures with a Nose–Hoover thermostat.[60] A plane wave energy cut-off of 300 eV was chosen for AIMD simulations of the supercells with a Gamma-centered 1 × 1 × 1 k-point grid, and the simulation supercell sizes were at least 10 Å along each lattice direction. The time step was set to 2 fs for a 100 ps AIMD trajectory.

The tracer diffusivity D was calculated as the mean square displacement over time interval Δt, known as the Einstein formula:

$$D = \frac{1}{2Nd\Delta t}\sum_{i=1}^{N}\left\langle |r_i(t+\Delta t) - r_i(t)|^2 \right\rangle_t \quad (2)$$

where $d = 3$ is the dimension of the diffusion system, N is the total number of diffusion ions, $r_i(t)$ is the displacement of the i-th ion at time t, and the bracket represents averaging over t.

The diffusivity and temperature satisfy the Arrhenius relationship:

$$D = D_0 \exp\left(-\frac{E_a}{k_B T}\right) \quad (3)$$

where k is the Boltzmann constant and T is the temperature in K. Activation energies E_a were determined from Arrhenius plots of the diffusivity.

The ionic conductivity was calculated according to the Nernst–Einstein relationship:

$$\sigma = \frac{nq^2}{k_B T} D$$

where n is the mobile ion volume density and q is the ionic charge.

The reorientation autocorrelation function $C(t)$[61] is defined as

$$C(t) = \langle u(t)\cdot u(t=0)\rangle \quad (4)$$

where $u(t)$ is a unit vector from the center of mass (*i.e.*, the position of the central Si atom) of the polyanion to a constituent anion (Se atom) at time t. < > denotes the averaged value across

all anions of the same species. The rate at which this function decays to zero reflects the reorientation rate of that species.

The power spectrum, for cation vibration and anion libration, was calculated *via* the Fourier transform of the velocity autocorrelation function, $\langle x(t')\cdot x(t'+t)\rangle$. x is the linear velocity (v_k) of the cation or angular velocity (w_k) of the anion. w_k was calculated *via*

$$w_k = \frac{r_k \times v_k}{{r_k}^2} \quad (5)$$

Here, r_k is the position vector for each anion atom relative to the central of mass of the polyanion.[28,42]

The Green–Kubo formula

$$D = \frac{1}{3N}\sum_i^N \int_0^\infty \langle x_i(t')x_i(t'+t)\rangle \mathrm{d}t \quad (6)$$

Here, D is the translational diffusivity or rotational diffusivity, and x_i is the linear velocity (v_k) of the cation or angular velocity (w_k) of the anion.

Author contributions

H. Z. designed and guided this research; Y. Y. performed the DFT calculations and wrote the paper; Z. X., C. G., and R. O. revised the paper and made suggestions. All authors discussed and commented on the paper.

Conflicts of interest

There are no conflicts to declare.

Acknowledgements

This work was supported by the National Natural Science Foundation of China (52072240), and the Materials Genome Initiative Center at Shanghai Jiao Tong University. All simulations were performed at the Shanghai Jiao Tong University High Performance Computing Center.

References

1 N. Kamaya, *et al.*, A lithium superionic conductor, *Nat. Mater.*, 2011, **10**, 682–686.
2 J. B. Goodenough and K.-S. Park, The Li-ion rechargeable battery: a perspective, *J. Am. Chem. Soc.*, 2013, **135**, 1167–1176.
3 J. Janek and W. G. Zeier, A solid future for battery development, *Nat. Energy*, 2016, **1**, 16141.
4 Y. Wang, *et al.*, Development of solid-state electrolytes for sodium-ion battery–a short review, *Nano Mater. Sci.*, 2019, **1**, 91–100.
5 E. A. Wu, S. Banerjee, H. Tang, *et al.*, A stable cathode-solid electrolyte composite for high-voltage, long-cycle-life solid-state sodium-ion batteries, *Nat. Commun.*, 2021, **12**(1), 1–11.
6 Y. Wang, *et al.*, Design principles for solid-state lithium superionic conductors, *Nat. Mater.*, 2015, **14**(10), 1026–1031.
7 K. J. Jun, *et al.*, Lithium superionic conductors with corner-sharing frameworks, *Nat. Mater.*, 2022, 1–8.
8 X. He, *et al.*, Crystal structural framework of lithium super-ionic conductors, *Adv. Energy Mater.*, 2019, **9**(43), 1902078.
9 X. He, Y. Zhu and Y. Mo, Origin of fast ion diffusion in super-ionic conductors, *Nat. Commun.*, 2017, **8**(1), 1–7.
10 Z. Zhang, Z. Zou, K. Kaup, R. Xiao, S. Shi, M. Avdeev and L. Chen, Correlated migration invokes higher Na^+-ion conductivity in NaSICON-type solid electrolytes, *Adv. Energy Mater.*, 2019, **9**(42), 1902373.
11 Z. Xu, X. Chen, H. Zhu and X. Li, Anharmonic Cation-Anion Coupling Dynamics Assisted Lithium-Ion Diffusion in Sulfide Solid Electrolytes, *Adv. Mater.*, 2022, 2207411.
12 S. Muy, R. Schlem, Y. Shao-Horn and W. G. Zeier, Phonon–ion interactions: Designing ion mobility based on lattice dynamics, *Adv. Energy Mater.*, 2021, **11**(15), 2002787.
13 G. Krenzer, C. E. Kim, K. Tolborg, B. J. Morgan and A. Walsh, Anharmonic lattice dynamics of superionic lithium nitride, *J. Mater. Chem. A*, 2022, **10**(5), 2295–2304.
14 Z. Xu, X. Chen, R. Chen, X. Li and H. Zhu, Anion charge and lattice volume dependent lithium ion migration in compounds with fcc anion sublattices, *npj Comput. Mater.*, 2020, **6**(1), 1–8.
15 Z. Xu and H. Zhu, Anion charge and lattice volume maps for searching lithium superionic conductors, *Chem. Mater.*, 2020, **32**(11), 4618–4626.
16 B. Zhang, R. Tan, L. Yang, J. Zheng, K. Zhang, S. Mo and F. Pan, Mechanisms and properties of ion-transport in inorganic solid electrolytes, *Energy Storage Mater.*, 2018, **10**, 139–159.
17 T. H. Wan and F. Ciucci, Ab Initio Study of the Defect Chemistry and Substitutional Strategies for Highly Conductive Li3YX6 (X= F, Cl, Br, and I) Electrolyte for the Application of Solid-State Batteries, *ACS Appl. Energy Mater.*, 2021, **4**(8), 7930–7941.
18 Y. Yang and H. Zhu, Effects of F and Cl Doping in Cubic Li7La3Zr2O12 Solid Electrolyte: A First-Principles Investigation, *ACS Appl. Energy Mater.*, 2022, **5**, 15086–15092.
19 Z. Zhang and L. F. Nazar, Exploiting the paddle-wheel mechanism for the design of fast ion conductors, *Nat. Rev. Mater.*, 2022, **7**(5), 389–405.
20 M. Jansen, Volume effect or paddle-wheel mechanism-fast alkali-metal ionic conduction in solids with rotationally disordered complex anions, *Angew. Chem., Int. Ed.*, 1991, **30**, 1547–1558.
21 D. Wilmer, K. Funke, M. Witschas, R. D. Banhatti, M. Jansen, G. Korus and R. E. Lechner, Anion reorientation in an ion conducting plastic crystal–coherent quasielastic neutron scattering from sodium ortho-phosphate, *Phys. B*, 1999, **266**(1–2), 60–68.
22 L. Karlsson and R. McGreevy, Mechanisms of ionic conduction in Li2SO4 and LiNaSO4: paddle wheel or percolation?, *Solid State Ionics*, 1995, **76**, 301–308.
23 Z. Xu and Y. Xia, Progress, challenges and perspectives of computational studies on glassy superionic conductors for

solid-state batteries, *J. Mater. Chem. A*, 2022, **10**, 11854–11880.

24 I. Hanghofer, B. Gadermaier, and H. M. R. Wilkening, "Fast Rotational Dynamics in Argyrodite-Type Li6PS5X (X: Cl, Br, I) as Seen by 31P Nuclear Magnetic Relaxation—On Cation–Anion Coupled Transport in Thiophosphates,", *Chemistry of Materials*, American Chemical Society, 2019, vol. 31, pp. 4591–4597.

25 A. Y. Song, K. Turcheniuk, J. Leisen, Y. Xiao, L. Meda, O. Borodin and G. Yushin, Understanding Li-Ion Dynamics in Lithium Hydroxychloride (Li2OHCl) Solid State Electrolyte via Addressing the Role of Protons, *Adv. Energy Mater.*, 2020, **10**(8), 1903480.

26 F. Wang, H. A. Evans, K. Kim, L. Yin, Y. Li, P. C. Tsai and Y. M. Chiang, Dynamics of hydroxyl anions promotes lithium ion conduction in antiperovskite Li2OHCl, *Chem. Mater.*, 2020, **32**(19), 8481–8491.

27 N. Verdal, T. J. Udovic, V. Stavila, W. S. Tang, J. J. Rush and A. V. Skripov, Anion reorientations in the superionic conducting phase of Na2B12H12, *J. Phys. Chem. C*, 2014, **118**(31), 17483–17489.

28 Z. Zhang, P. N. Roy, H. Li, M. Avdeev and L. F. Nazar, Coupled cation–anion dynamics enhances cation mobility in room-temperature superionic solid-state electrolytes, *J. Am. Chem. Soc.*, 2019, **141**(49), 19360–19372.

29 Z. Zhang, H. Li, K. Kaup, L. Zhou, P. N. Roy and L. F. Nazar, Targeting superionic conductivity by turning on anion rotation at room temperature in fast ion conductors, *Matter*, 2020, **2**(6), 1667–1684.

30 H. Fang and P. Jena, Argyrodite-type advanced lithium conductors and transport mechanisms beyond peddle-wheel effect, *Nat. Commun.*, 2022, **13**(1), 1–11.

31 M. B. Effat, J. Liu, Z. Lu, T. H. Wan, A. Curcio and F. Ciucci, Stability, elastic properties, and the Li transport mechanism of the protonated and fluorinated antiperovskite lithium conductors, *ACS Appl. Mater. Interfaces*, 2020, **12**(49), 55011–55022.

32 Y. Sun, B. Ouyang, Y. Wang, Y. Zhang, S. Sun, Z. Cai, V. Lacivita, Y. Guo and G. Ceder, Enhanced ionic conductivity and lack of paddle-wheel effect in pseudohalogen-substituted Li argyrodites, *Matter*, 2022, **5**(12), 4379–4395.

33 A. Jain, *et al.*, Commentary: The materials project: a materials genome approach to accelerating materials innovation, *APL Mater.*, 2013, **1**, 011002.

34 S. P. Ong, *et al.*, The Materials Application Programming Interface (API): a simple, flexible and efficient API for materials data based on REpresentational State Transfer (REST) principles, *Comput. Mater. Sci.*, 2015, **97**, 209–215.

35 G. Bergerhoff, R. Hundt, R. Sievers and I. D. Brown, The inorganic crystal structure data base, *J. Chem. Inf. Comput. Sci.*, 1983, **23**, 66–69.

36 Y. Y. Lin, J. Qu, W. J. Gustafson, P. C. Kung, N. Shah, S. Shrivastav and N. H. Perry, Coordination flexibility as a high-throughput descriptor for identifying solid electrolytes with Li+ sublattice disorder: A computational and experimental study, *J. Power Sources*, 2023, **553**, 232251.

37 W. Sun, S. T. Dacek, S. P. Ong, G. Hautier, A. Jain, W. D. Richards and G. Ceder, The thermodynamic scale of inorganic crystalline metastability, *Sci. Adv.*, 2016, **2**(11), e1600225.

38 H. Preishuber-Pflügl and K. O. Klepp, Crystal structure of tetrasodium tetraselenidosilicate (IV), Na4SiSe4, *Z. fur Krist. - New Cryst. Struct.*, 2003, **218**(4), 383–384.

39 J. B. Goodenough and Y. Kim, Challenges for Rechargeable Li Batteries, *Chem. Mater.*, 2010, **22**, 587–603.

40 S. P. Ong, L. Wang, B. Kang and G. Ceder, Li-Fe-P-O2 Phase Diagram from First Principles Calculations, *Chem. Mater.*, 2008, **20**(5), 1798–1807.

41 Y. Zhu and Y. Mo, Materials design principles for air-stable lithium/sodium solid electrolytes, *Angew. Chem., Int. Ed.*, 2020, **59**(40), 17472–17476.

42 J. G. Smith and D. J. Siegel, Ion Migration Mechanisms in the Sodium Sulfide Solid Electrolyte Na_{3-x} Sb_{1-x} W *x* S4, *Chem. Mater.*, 2022, **34**(9), 4166–4171.

43 Z. Zhu, I. H. Chu, Z. Deng and S. P. Ong, Role of Na+ interstitials and dopants in enhancing the Na+ conductivity of the cubic Na3PS4 superionic conductor, *Chem. Mater.*, 2015, **27**(24), 8318–8325.

44 M. Burbano, D. Carlier, F. Boucher, B. J. Morgan and M. Salanne, Sparse cyclic excitations explain the low ionic conductivity of stoichiometric $Li_7La_3Zr_2$ O12, *Phys. Rev. Lett.*, 2016, **116**, 1–6.

45 A. S. Keys, L. O. Hedges, J. P. Garrahan, S. C. Glotzer and D. Chandler, Excitations are localized and relaxation is hierarchical in glass-forming liquids, *Phys. Rev. X*, 2011, **1**, 1–15.

46 J. G. Smith and D. J. Siegel, Low-temperature paddlewheel effect in glassy solid electrolytes, *Nat. Commun.*, 2020, **11**(1), 1–11.

47 L. Börjesson and L. M. Torell, Contrasting behavior of the SO4 symmetric Rahman modes in high and low conducting sulfates, *Proc. – Electrochem. Soc.*, 1986, **1**, 21–28.

48 S. P. Ong, W. D. Richards, A. Jain, G. Hautier, M. Kocher, S. Cholia and G. Ceder, Python Materials Genomics (pymatgen): A robust, open-source python library for materials analysis, *Comput. Mater. Sci.*, 2013, **68**, 314–319.

49 P. P. Ewald, *Ann. Phys.*, 1921, **64**, 253–287.

50 Y. Mo, S. P. Ong and G. Ceder, First principles study of the Li10GeP2S12 lithium super ionic conductor material, *Chem. Mater.*, 2012, **24**(1), 15–17.

51 Z. Zhu, H. Tang, J. Qi, X. G. Li and S. P. Ong, Design Principles for Cation-Mixed Sodium Solid Electrolytes, *Adv. Energy Mater.*, 2021, **11**(7), 2003196.

52 Y. Wang, W. D. Richards, S. H. Bo, L. J. Miara and G. Ceder, Computational prediction and evaluation of solid-state sodium superionic conductors Na7P3X11 (X= O, S, Se), *Chem. Mater.*, 2017, **29**(17), 7475–7482.

53 X. Feng, P. H. Chien, Z. Zhu, I. H. Chu, P. Wang, M. Immediato-Scuotto and Y. Y. Hu, Studies of Functional Defects for Fast Na-Ion Conduction in Na3− yPS4− xClx with a Combined Experimental and Computational Approach, *Adv. Funct. Mater.*, 2019, **29**(9), 1807951.

54 W. Kohn and L. J. Sham, *Phys. Rev.*, 1965, **140**, A1133.

55 P. E. Blöchl, *Phys. Rev. B: Condens. Matter Mater. Phys.*, 1994, **50**, 17953.
56 J. P. Perdew, K. Burke and M. Ernzerhof, *Phys. Rev. Lett.*, 1996, **77**, 3865.
57 J. Heyd and G. E. Scuseria, Efficient hybrid density functional calculations in solids: Assessment of the Heyd–Scuseria–Ernzerhof screened Coulomb hybrid functional, *J. Chem. Phys.*, 2004, **121**, 1187–1192.
58 S. Baroni, S. De Gironcoli, A. Dal Corso and P. Giannozzi, Phonons and Related Crystal Properties from Density-Functional Perturbation Theory, *Rev. Mod. Phys.*, 2001, **73**, 515.
59 A. Togo and I. Tanaka, First Principles Phonon Calculations in Materials Science, *Scr. Mater.*, 2015, **108**, 1–5.
60 W. G. Hoover, *Phys. Rev.*, A1985, **31**, 1695.
61 J. P. Hansen and I. R. McDonald *Theory of Simple Liquids*, Academic Press, 2013.